

---

This is an electronic reprint of the original article.  
This reprint may differ from the original in pagination and typographic detail.

Saeedian, Meysam; Eskandari, Bahman; Taheri, Shamsodin; Hinkkanen, Marko;  
Pouresmaeil, Edris

## **A Control Technique Based on Distributed Virtual Inertia for High Penetration of Renewable Energies Under Weak Grid Conditions**

*Published in:*  
IEEE Systems Journal

*DOI:*  
[10.1109/JSYST.2020.2997392](https://doi.org/10.1109/JSYST.2020.2997392)

Published: 01/06/2021

*Document Version*  
Peer-reviewed accepted author manuscript, also known as Final accepted manuscript or Post-print

*Please cite the original version:*  
Saeedian, M., Eskandari, B., Taheri, S., Hinkkanen, M., & Pouresmaeil, E. (2021). A Control Technique Based on Distributed Virtual Inertia for High Penetration of Renewable Energies Under Weak Grid Conditions. *IEEE Systems Journal*, 15(2), 1825-1834. Article 9112269. <https://doi.org/10.1109/JSYST.2020.2997392>

© 2020 IEEE. This is the author's version of an article that has been published by IEEE. Personal use of this material is permitted. Permission from IEEE must be obtained for all other uses, in any current or future media, including reprinting/republishing this material for advertising or promotional purposes, creating new collective works, for resale or redistribution to servers or lists, or reuse of any copyrighted component of this work in other works.

---

This is an electronic reprint of the original article.  
This reprint may differ from the original in pagination and typographic detail.

Saeedian, Meysam; Eskandari, Bahman; Taheri, Shamsodin; Hinkkanen, Marko;  
Pouresmaeil, Edris

## **A Control Technique Based on Distributed Virtual Inertia for High Penetration of Renewable Energies Under Weak Grid Conditions**

*Published in:*  
IEEE Systems Journal

*DOI:*  
[10.1109/JSYST.2020.2997392](https://doi.org/10.1109/JSYST.2020.2997392)

E-pub ahead of print: 01/01/2020

*Document Version*  
Peer reviewed version

*Please cite the original version:*  
Saeedian, M., Eskandari, B., Taheri, S., Hinkkanen, M., & Pouresmaeil, E. (2020). A Control Technique Based on Distributed Virtual Inertia for High Penetration of Renewable Energies Under Weak Grid Conditions. *IEEE Systems Journal* . <https://doi.org/10.1109/JSYST.2020.2997392>

# A Control Technique Based-on Distributed Virtual Inertia for High Penetration of Renewable Energies under Weak Grid Conditions

Meysam Saeedian, Bahman Eskandari, Shamsodin Taheri, *Senior Member, IEEE*, Marko Hinkkanen, *Senior Member, IEEE*, Edris Pouresmaeil, *Senior Member, IEEE*

**Abstract**— Distributed virtual inertia is an approach of providing synthetic inertia in small-scale modern grids dominated by converter-based generators. In this method, the inertial response of synchronous machines is emulated by the energy stored in the dc-link capacitors of grid-tied converters. Nonetheless, it results in instability of the interfaced converter in weak grids. To overcome this problem and get the most benefit out of the acceptable dc-link capacitor voltage deviations, a new compensation technique is proposed in this paper. The grid-interactive converter in the presented framework is controlled in the current control mode, compositing of two conventional inner and outer control loops, distributed virtual inertia controller and a novel compensator. The detailed small-signal representation of the whole control scheme in state-space form is derived. Then, it is revealed that the coupling between  $d$ - and  $q$ - axis controllers introduced by the distributed virtual inertia gain and its differential operator gives rise to the system instability in weak grids, which can be eliminated through the ancillary compensator. The time-domain simulation model is built to confirm the efficacy of the proposed control technique. The results depict that the ancillary active power provided by the proposed approach during frequency disturbance is 14% of the converter power rating of 20 kW, which yields the improvement of frequency rate of change by 18.82%.

**Index Terms**— Distributed virtual inertia, weak grids, phase-locked loop dynamics, frequency support functionality.

## NOMENCLATURE

### Abbreviations:

<i>DVI</i>	Distributed virtual inertia
<i>POI</i>	Point of interconnection
<i>PWM</i>	Pulse width modulation
<i>RESs</i>	Renewable energy sources
<i>RoCoF</i>	Rate of change of frequency
<i>SGs</i>	Synchronous generators
<i>SRF</i>	Synchronous reference frame
<i>VSC</i>	Voltage sourced converter

### Variables:

$i$	Current flowing into the grid
$i_w$	Current flowing through the $LC$ filter
$P_{out}$	The output power of VSC
$u_g$	The grid voltage
$u_p$	The POI voltage

$u_t$	Modulation voltage at the VSC output
$u_{dc}$	DC-link capacitor voltage
$\omega$	Angular frequency of the grid measured by the PLL
$\delta$	Synchronization angle

### Parameters:

$C_{dc}, C_f$	DC-link and filter capacitances
$k$	DVI gain
$k_{db}, k_q$	The compensators gain corresponding to $d$ - and $q$ - axes
$k_{ppl}, k_{ipll}$	The proportional and integral gains of the PLL controller
$k_{pi}, k_{ii}$	The proportional and integral gains of the inner-loop controller
$k_{pu}, k_{iu}$	The proportional and integral gains of the outer-loop controller
$P_{in}$	The input power of VSC
$R_f, L_f$	Resistance and inductance of the filter
$R_g, L_g$	Resistance and inductance of the grid
$U_{pd0}$	Nominal POI voltage in $d$ -axis
$u_{dc}^*$	DC-link voltage reference
$\omega_0$	Nominal angular frequency of the grid
$\omega_{db}, \omega_q$	The compensators cut-off frequency corresponding to $d$ - and $q$ - axes

### Indices:

$dq, dq^*$	Synchronous reference frames corresponding to the grid voltage and the VSC controller
------------	---

## I. INTRODUCTION

**P**OWER systems dominated by conventional SGs are robust against frequency deviations introduced by disturbances, typically loss of generation or stochastic demand fluctuations. This is because the kinetic energy preserved in the rotational mass of the SGs can mitigate the power imbalance between generation and demand in the timescale of seconds [1], [2]. In other words, the primary frequency regulation of the real SGs imposes a limit on the frequency oscillations and slow down the grid frequency dynamics. Lack of the kinetic energy might lead to undesirable situations such as pole slipping and catastrophic failure of SGs, under frequency load shedding activation or

even cascading outages after perturbations [3], [4].

Nonetheless, ever-increasing electricity demand and the concerns regarding global warming have led to speeding up the integration of RESs into power systems [5]-[7]. VSCs are the vital interface in these systems, which have neither rotational inertia nor damping characteristics of the conventional SGs [8]-[10]. Power systems can be more vulnerable to the aforesaid risks in the case where the converter-based renewable energy generators provide a considerable portion of the demand. Hence, further integration of RESs into power systems is not possible without modifying present grid-tied converter control techniques or employing alternative approaches [11], [12]. Generally, the system frequency stability is assessed with two more sited indices: 1) frequency nadir or maximum frequency deviation with regard to the nominal value, and 2) rate of frequency change in a period (RoCoF). It is worth mentioning that the inertia emulation (also known as synthetic inertia) is defined as the contribution made by a converter based-generating unit to emulate the kinetic energy stored in the rotors of real SGs aimed at restraining the grid frequency fluctuations. The more inertia, the better frequency regulation during transient time [13].

#### A. Literature Survey and Research Gap

Extensive research has been presented in the literature to address foregoing concerns regarding lack of inertia characteristic in the power systems dominated by RESs and complying with new grid codes [14]-[24]. Changing the requirements of RoCoF withstand capabilities of the SGs is a straightforward approach, which has been implemented by the system operators in Ireland [14]. However, this method does not solve the inertia shortage in power systems. Moreover, the high costs corresponding to generator testing can bound its applications. Employing synchronous condensers is another solution of inertia augmentation [15]. The kinetic energy stored in the rotor of a synchronous condenser contributes to the total inertia of the power system and is thus beneficial from a frequency/voltage control perspective. Nevertheless, high capital and maintenance costs have led to preventing their widespread applications. Inspired by the dynamics of real SGs, the concept of virtual synchronous machines has been introduced for the first time in 2007 [16]. The article described a new power electronic-based approach of integrating renewable energies, making them appear as the electromechanical synchronous machines. Thereafter, the analogous concepts named Synchronverter and Inducverter have been developed in [17] and [18], respectively. Grid-scale energy storage devices, e.g. ultra-capacitors and battery banks, gained popularity in power systems with the aim of frequency support and output power ramp-rate mitigation of RESs. In [19], an ultra-capacitor has been applied to smooth the output power of RESs and primary frequency regulation during a contingency. The research work conducted in [20] applies super-capacitor to enhance the frequency stability, in which droop characteristic is paralleled with an integral controller and a distribution function. The authors in [21] proposed a multiple

services provision based battery energy storage system (BESS) in the presence of uncertainties. Reference [22] enhanced a control method for BESSs in autonomous microgrids with high penetration of RESs. In the developed technique, a frequency controller composed of a droop control and inertia emulation function governs the active power of the BESS. A promising method called Distributed Virtual Inertia (DVI) has been introduced in [3], [23] and [24] for increasing inertia in modern power systems augmented with a large number of grid-tied power converters. In this approach, the dc capacitors inhered in the dc-side of the power converters act as energy buffers, potentially providing frequency support during perturbations. Compared to the foregoing techniques, the DVI provides primary frequency regulation without imposing the extra cost on the grid-interactive VSCs hardware [3], [23].

Despite numerous studies that demonstrate how synthetic inertia can be emulated through various mechanisms, few of them address the question of “where” to place the virtual inertia devices in power grids to increase its resilience and system efficiency [25], [26]. Hence, the aforesaid topic, i.e. *optimizing the inertia placement problem*, is the research gap in the area of high penetration of RESs and needs further studies.

#### B. Aims and Contributions

The contributions of this paper compared with the existing research works are summarized as:

- 1) A complete small-signal state-space realization of the grid-interfaced VSC, compositing of  $dq$  current control loops, dc-side voltage controller, DVI controller, PLL dynamics, and reference frame transformation is derived in details.
- 2) Then, it is revealed that the VSC augmented with the DVI functionality (proposed in [3]) induces instability to the control system in weak grids due to the coupling between  $d$ - and  $q$ - control axes introduced by the gain and differential operator of the DVI function.
- 3) To overcome this instability problem and get the most benefit out of the acceptable dc-link voltage deviations, a new compensation technique is proposed and applied to the  $dq$  control loops. Therefore, the proposed control scheme provides the maximum DVI support while the system remains stable in weak grids, which is the main contribution of this paper.

#### C. Paper Organization

The rest of this paper is organized as follows: Section II presents the diagram and mathematical model of the grid-tied VSC controlled in the current control mode. The small-signal state-space modeling of the interfaced converter is then derived in Section III, where the instability problem of the VSC equipped with the DVI functionality in weak grids is further elaborated. Section IV includes the proposed compensator and its design process with the aim of stability enhancement. The analytical model and efficacy of the proposed control scheme is then verified by the simulations provided in Section V. The paper ends with the conclusions in Section VI.

## II. GRID-INTERACTIVE VSC AUGMENTED WITH DVI TECHNIQUE

### A. Control Platform of the VSC

Fig. 1 depicts the single-line diagram of the grid-tied VSC with an  $LC$  filter under weak grid condition. The dc-side of the converter can be fed by RESs, e.g., photovoltaic or wind farm. The dc-capacitor applied to the dc-side is essential for voltage support and harmonic filtering. In the DVI concept, this capacitor acts as the energy buffer for increasing grid inertia. The full design procedure for gaining a predetermined amount of synthetic inertia by the DVI approach is provided in [3]. The high-order harmonics introduced by the switching process can be mitigated by the interface  $LC$  filter. The grid is modeled with the equivalent Thevenin circuit and internal impedance of  $R_g$  and  $L_g$ .

Due to operation of the synchronization unit (typically a SRF-PLL), the whole system comprises two  $dq$  reference frames: one is for the grid defined by the POI voltage ( $dq$ ), and the other one is for the controller defined by the PLL ( $dq^c$ ) [27], [28]. In steady state operation, both reference frames are aligned and adhered to one another. When a small contingency occurs (e.g. demand fluctuations), the synchronization angle ( $\delta$ ) oscillates to resynchronize the VSC with the grid. In other words, the two frames are no longer aligned and  $dq^c$  lags  $dq$  frame due to the dynamics of the PLL [Fig. 2(a)]. Note that,  $\Delta$  refers to a small perturbation of the corresponding variable.

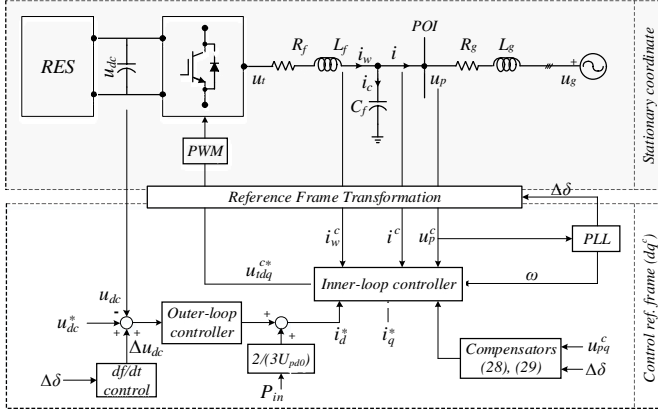


Fig. 1. The proposed control scheme of the grid-tied VSC augmented with DVI functionality.

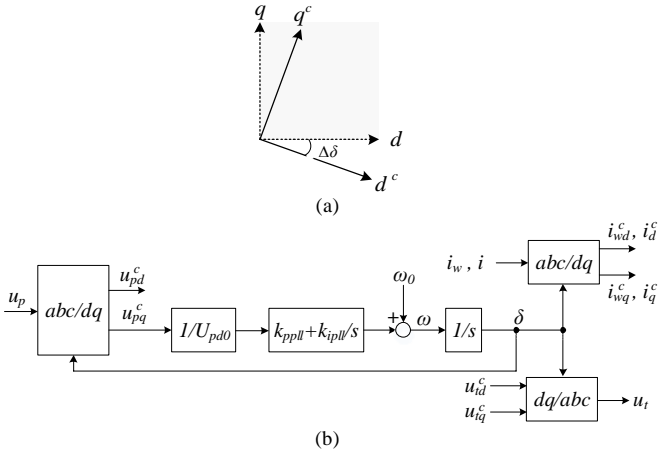


Fig. 2. (a) Grid and controller reference frames, (b) diagram of the SRF-PLL.

To precisely model the dynamics introduced by the PLL, the measured quantities of  $u_p$ ,  $i_w$  and  $i$  in the  $dq$  frame must be transformed to the  $dq^c$  frame for feedback control purpose as illustrated in Fig. 2(b). The control signals ( $u_{idq}^{c*}$ ) generated by the feedback loops are then retransformed to the grid reference frame. Presume that the difference angle between two frames is small; the mathematical model of this process can be characterized by:

$$\underline{u}_p^c = (1 - j\delta)\underline{u}_p \quad (1)$$

$$\underline{i}^c = (1 - j\delta)\underline{i} \quad (2)$$

$$\underline{i}_w^c = (1 - j\delta)\underline{i}_w \quad (3)$$

$$\underline{u}_t = (1 + j\delta)\underline{u}_t^c \quad (4)$$

### B. System Modeling in State-Space Form

The VSC control system of Fig. 1 is analyzed and expressed in terms of nonlinear mathematical equations in this subsection. The equations are then linearized around an operating point for stability analysis in Section III [29].

#### 1) Phase-Locked Loop

The PLL adopted in this paper is based on regulating the normalized  $q$ -axis component of the POI voltage to zero by means of a PI controller as illustrated in Fig. 2(b) [30]. Two state variables are defined associated with the PLL and its model is described as:

$$\dot{\delta} = \omega = \omega_0 + \frac{k_{pll}}{U_{pd0}} u_{pq}^c + \varphi_\delta \quad (5)$$

where  $\dot{\delta}$  is the time-derivative of the synchronization angle and  $\varphi_\delta$  is defined as:

$$\varphi_\delta = \frac{k_{ipll}}{U_{pd0}} \int u_{pq}^c dt. \quad (6)$$

#### 2) DC-bus Dynamics

Neglecting the energy loss in the VSC, the equation describing the dynamics of the dc-link is brought in (7) based on the power balance between two sides of the converter [31]:

$$P_{in} - P_{out} = C_{dc} u_{dc} \dot{u}_{dc} \quad (7)$$

in which  $\dot{u}_{dc}$  is the time-derivative of the dc-link capacitor voltage and  $P_{in}$  is the input power of VSC. Followed by the instantaneous power equation in the synchronous reference frame, the VSC output power  $P_{out}$  is obtained as:

$$P_{out} = \frac{3}{2} (u_{pd} i_d + u_{pq} i_q). \quad (8)$$

From (7) and (8), the state-space representation of the dc-link dynamics is then formed as:

$$\dot{u}_{dc} = \frac{P_{in} - \frac{3}{2} (u_{pd} i_d + u_{pq} i_q)}{C_{dc} u_{dc}}. \quad (9)$$

#### 3) LC Filter and Power Grid

The filter applied to the VSC system is depicted in Fig. 1. Without any major inaccuracies, we can assume that the command signals generated by the feedback loops appear in the input side of the filter after retransforming from the  $dq^c$  frame to  $dq$  frame (i.e.  $u_{tdq} = u_{tdq}^*$ ) [32]. This approach only neglects the

losses in the VSC power switches. Hence, the equations describing the ac-side dynamics of the VSC are established as:

$$\dot{i}_{wd} = \frac{1}{L_f} u_{td} - \frac{1}{L_f} u_{pd} - \frac{R_f}{L_f} i_{wd} + i_{wq} \left( \omega_0 + \frac{k_{ppll}}{U_{pd0}} u_{pq}^c + \varphi_\delta \right) \quad (10)$$

$$\dot{i}_{wq} = \frac{1}{L_f} u_{tq} - \frac{1}{L_f} u_{pq} - \frac{R_f}{L_f} i_{wq} - i_{wd} \left( \omega_0 + \frac{k_{ppll}}{U_{pd0}} u_{pq}^c + \varphi_\delta \right) \quad (11)$$

$$\dot{u}_{pd} = \frac{1}{C_f} i_{wd} - \frac{1}{C_f} i_d + u_{pq} \left( \omega_0 + \frac{k_{ppll}}{U_{pd0}} u_{pq}^c + \varphi_\delta \right) \quad (12)$$

$$\dot{u}_{pq} = \frac{1}{C_f} i_{wq} - \frac{1}{C_f} i_q - u_{pd} \left( \omega_0 + \frac{k_{ppll}}{U_{pd0}} u_{pq}^c + \varphi_\delta \right) \quad (13)$$

$$\dot{i}_d = \frac{1}{L_g} u_{pd} - \frac{R_g}{L_g} i_d - \frac{1}{L_g} u_{gd} + i_q \left( \omega_0 + \frac{k_{ppll}}{U_{pd0}} u_{pq}^c + \varphi_\delta \right) \quad (14)$$

$$\dot{i}_q = \frac{1}{L_g} u_{pq} - \frac{R_g}{L_g} i_q - \frac{1}{L_g} u_{gq} - i_d \left( \omega_0 + \frac{k_{ppll}}{U_{pd0}} u_{pq}^c + \varphi_\delta \right). \quad (15)$$

#### 4) Inner-Loop Controller

The internal current controller indicated in Fig. 3 is implemented as a pair of PI controllers ( $G_i(s) = k_{pi} + k_{ii}/s$ ) with POI voltage feedforward terms and cross-axis decoupling loops, which can be represented mathematically as:

$$u_{td}^c = u_{pd}^c - \omega L_f i_{wq}^c + k_{pi} (i_d^* - i_d^c) + \varphi_{id} \quad (16)$$

$$u_{tq}^c = u_{pq}^c + \omega L_f i_{wd}^c + k_{pi} (i_q^* - i_q^c) + \varphi_{iq} \quad (17)$$

where  $\varphi_{id}$  and  $\varphi_{iq}$  are defined, respectively as:

$$\varphi_{id} = k_{ii} \int (i_d^* - i_d^c) dt \quad (18)$$

$$\varphi_{iq} = k_{ii} \int (i_q^* - i_q^c) dt. \quad (19)$$

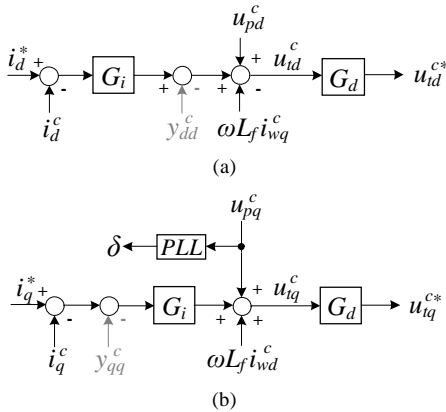


Fig. 3. The inner-loop controllers, (a)  $d$ -axis, (b)  $q$ -axis.

Note that the  $q$ -axis reference current ( $i_q^*$ ) is dependent on the requirement of the reactive power compensation. The controller computational delay and the PWM updates are modeled as a dead time  $T_d$  through a first-order lag transfer function [28], [33]:

$$G_d(s) = \frac{1}{1 + T_d s} \quad (20)$$

where  $T_d = 3/(2f_s)$  with  $f_s$  being the sampling frequency.

According to Fig. 3 and (20), the voltage command signals ( $u_{tdq}^{c*}$ ) generated by the feedback loops are obtained as:

$$\dot{u}_{td}^{c*} = 2f_s (u_{td}^c - u_{td}^{c*})/3 \quad (21)$$

$$\dot{u}_{tq}^{c*} = 2f_s (u_{tq}^c - u_{tq}^{c*})/3. \quad (22)$$

#### 5) Outer-Loop Controller Equipped with DVI Functionality

The dc-link voltage is set to its reference value through regulating the  $d$ -axis reference current (i.e.  $i_d^*$ ), which is achieved by a PI controller ( $G_u(s) = -k_{pu} - k_{iu}/s$ ) as depicted in Fig. 4. The employed DVI technique also links frequency deviations ( $\Delta\omega$ ) to the dc-link voltage such that any  $\Delta\delta$  results in the dc-bus voltage changes. Note that,  $\omega$  is equal to the time-derivative of  $\delta$  [Fig. 2(b)]. Then, the mathematical model of the outer-loop controller is obtained as:

$$\dot{i}_d^* = k_{pv} \left[ u_{dc} - u_{dc}^* - k \left( \frac{k_{ppll}}{U_{pd0}} u_{pq}^c + \varphi_\delta \right) \right] + \varphi_u \quad (23)$$

where  $\varphi_u$  is:

$$\varphi_u = k_{iu} \int \left[ u_{dc} - u_{dc}^* - k \left( \frac{k_{ppll}}{U_{pd0}} u_{pq}^c + \varphi_\delta \right) \right] dt. \quad (24)$$

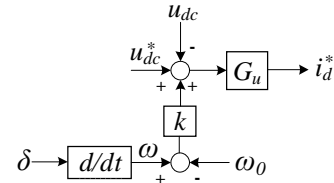


Fig. 4. The outer-loop controller equipped with DVI function.

### III. SMALL-SIGNAL MODELING

In this section, the detailed small-signal model of the grid-interfaced converter system in Fig. 1 is obtained to demonstrate the impact of the DVI gain on the system stability in weak grids. The foregoing equations (5)-(24) are linearized around operating points (denoted by subscript 0) and the small-signal state-space realization of the closed-loop system is derived as:

$$[\Delta \dot{x}_{uncomp}] = [A_{uncomp}] [\Delta x_{uncomp}] + [B] [\Delta u] \quad (25)$$

in which  $\Delta x_{uncomp}$  and  $\Delta u$  are defined, respectively as:

$$\Delta x_{uncomp} = \begin{bmatrix} \Delta \delta & \Delta \varphi_\delta & \Delta u_{td} & \Delta u_{tq} & \Delta i_{wd} & \Delta i_{wq} & \Delta u_{pd} \\ \Delta u_{pq} & \Delta i_d & \Delta i_q & \Delta u_{dc} & \Delta \varphi_u & \Delta \varphi_{id} & \Delta \varphi_{iq} \end{bmatrix}^T \quad (26)$$

$$\Delta u = [\Delta P_{in} \quad \Delta i_q^*]^T. \quad (27)$$

The state variables  $\Delta \varphi_\delta$ ,  $\Delta \varphi_u$ ,  $\Delta \varphi_{id}$  and  $\Delta \varphi_{iq}$  denote integral terms of the PLL, outer-loop controller,  $d$ - and  $q$ -internal loop controllers, respectively. The system parameters are provided in Appendix A and the matrices corresponding to the state-space realization are presented in Appendix B.

Fig. 5 depicts the migration trend of VSC system eigenvalues with respect to the coefficient  $k$  when the grid inductance  $L_g$  is 2 mH. It is clear that the conjugate pole pair ( $\lambda_I$ ) moves towards the unstable region as the DVI gain  $k$  increases. The dominant pole pair ( $\lambda_I$ ) corresponds to the coupling between  $d$ - and  $q$ -

axes introduced by the synthetic inertia loop (Fig. 4). The converter system becomes unstable even with a small coefficient  $k$  when the grid is weaker (i.e. larger  $L_g$ ). Fig. 6 illustrates the system eigenvalues for different  $k$  and  $L_g$ . As an example, with  $L_g=1$  mH the system is still stable for  $k=15$  V.s. However, increasing  $L_g$  while  $k$  is constant leads to the instability of the VSC system.

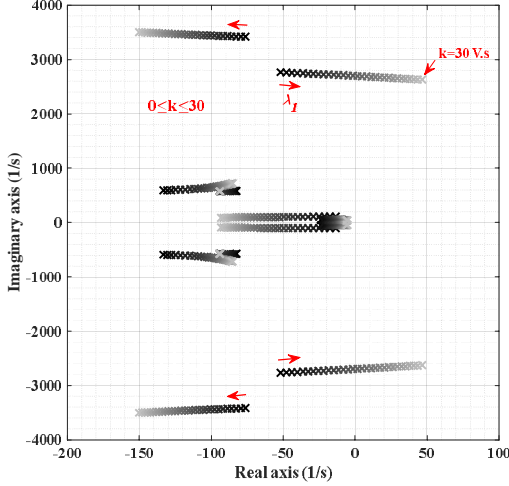


Fig. 5. Eigenvalues' migration in terms of different DVI gain ( $L_g=2$  mH).

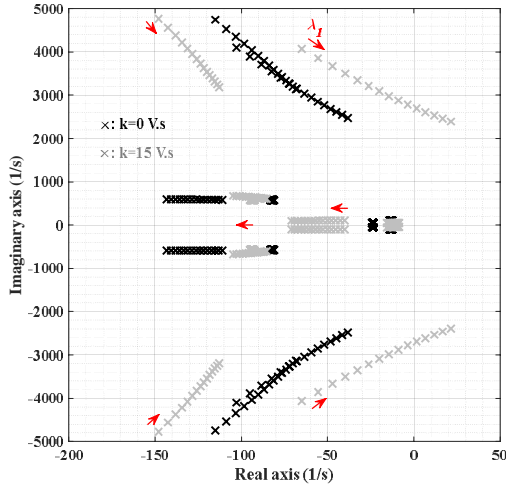


Fig. 6. Eigenvalues' migration in terms of different DVI gain and grid inductance  $L_g$  ( $L_g=1$  mH; 0.1 mH; 2.4 mH).

#### IV. PROPOSED COMPENSATOR

To overcome the instability issue caused by the DVI gain and get the most benefit out of the acceptable dc-link voltage deviations for primary frequency support, a new compensation technique is proposed. As demonstrated in Fig. 3, the compensation signals  $y_{dd}^c(s)$  and  $y_{qq}^c(s)$  are added to the  $d$ - and  $q$ - channels, respectively. These ancillary signals are defined as follows:

$$y_{dd}^c = \frac{-k_d \omega_d}{s + \omega_d} (s\delta - \omega_0) \quad (28)$$

$$y_{qq}^c = \frac{-k_q \omega_q}{s + \omega_q} u_{pq}^c. \quad (29)$$

The compensators are designed based on the fact that the coupling between  $d$ - and  $q$ - axes introduced by the gain and differential operator of the DVI function (see Figs. 3 and 4) is the dominant detrimental reason for the control system instability in weak grids. To counteract the adverse impact of the DVI loop on the system stability, the time-derivative of the PLL output (i.e.  $\dot{\delta}$ ) is applied to the compensator (28). Note that the ancillary compensator should not affect the  $d$ - axis control loop in the steady state. Hence,  $\dot{\delta} - \omega_0$  is selected as the input signal to the compensator (28), which is then passed through a low-pass filter with the cut-off frequency of  $\omega_d$  and the gain of  $k_d$  to attain  $y_{dd}^c(s)$ . Moreover, the PLL control variable  $u_{pq}^c$  is applied to a low-pass filter to obtain  $y_{qq}^c(s)$ , in which  $\omega_q$  is the cut-off frequency and  $k_q$  is the gain. It should be emphasized that the outputs of the compensators are zero during steady state operation. Thus, the tracking of the control variables is not affected by (28) and (29).

##### A. Small-Signal Model of the Proposed Compensator

According to (28) and (29), two state variables are added to the system modeled by (25). Thus, the small-signal representation of the compensator in state-space form is derived as:

$$[\Delta \dot{x}_c] = [A_{c4}] [\Delta x_c] + [A_{c3}] \Delta u_{pq} + [A_{c2}] \Delta \varphi_\delta + [A_{c1}] \Delta \delta \quad (30)$$

$$[\Delta y_{dd,qq}^c] = [C_c] [\Delta x_c] \quad (31)$$

in which  $\Delta x_c$  is:

$$[\Delta x_c] = [\Delta \gamma_{dd} \quad \Delta \gamma_{qq}]^T. \quad (32)$$

The model in (30) is then added to (25) in order to shape the compensated system as follow:

$$[\Delta \dot{x}_{comp}] = [A_{comp}] [\Delta x_{comp}]. \quad (33)$$

The matrices corresponding to (30), (31), and (33) are provided in Appendix B.

##### B. Stability Assessment and Compensators Design

The compensators design is conducted in two steps, 1) design of  $y_{dd}^c(s)$  and 2) design of  $y_{qq}^c(s)$  considering  $y_{dd}^c(s)$ . As the worst case, the DVI gain and grid inductance in all steps are set to 30 V.s and 2 mH, respectively (see Fig. 5).

###### 1) Design of $y_{dd}^c(s)$

At first, the small-signal model of the compensator  $y_{dd}^c(s)$  is added to (25). Fig. 7 depicts the corresponding impact on the VSC system dynamics as the gain  $k_d$  changes from zero to 2.7 V.s. As observed from this figure, the unstable conjugate pole pair ( $\lambda_1$ ) moves towards the stable region by increasing  $k_d$ . Notice, this trend occurs at a faster rate for higher values of the cut-off frequency  $\omega_d$ . Thus, the coefficients  $k_d=2.7$  V.s and  $\omega_d=1500$  rad/s are selected. At  $k=30$  V.s and  $L_g=2$  mH, the unstable eigenvalues ( $\lambda_1$ ) are relocated to  $-87 \pm 2915j$ , which are influenced (damped) by the state of the proposed compensator ( $\Delta \gamma_{dd}$ ). However, the impact of  $y_{dd}^c(s)$  on the controller system



leads to the movement of conjugate pole pair ( $\lambda_2$ ) towards the unstable region as the gain  $k_d$  reaches 2.7 V.s. This negative impact is eliminated by the proper design of  $y_{qq}^c(s)$  in the next step.

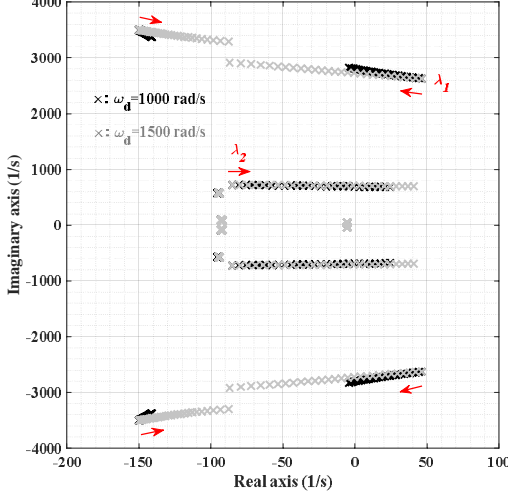


Fig. 7. The impact of  $y_{dd}^c(s)$  on the system dynamics.

## 2) Design of $y_{qq}^c(s)$

The small-signal stability of the VSC system in Fig. 1 is assessed when both compensators  $y_{dd}^c(s)$  and  $y_{qq}^c(s)$  are considered. Fig. 8 depicts the locus of the dominant modes when  $k_q$  varies from zero to 0.9 A/V. It is clear that changing the gain  $k_q$  has a minimal effect on the conjugate pole pair ( $\lambda_1$ ). As compared to Fig. 7, the proposed compensator  $y_{qq}^c(s)$  successfully relocates the unstable pole pair ( $\lambda_2$ ) to the left-hand side of the imaginary axis in the complex  $s$ -plane. Again, this trend occurs at a faster rate for higher values of the cut-off frequency  $\omega_q$ . Accordingly, the coefficients  $k_q=0.9$  A/V and  $\omega_q=300$  rad/s are selected for the compensator  $y_{qq}^c(s)$ .

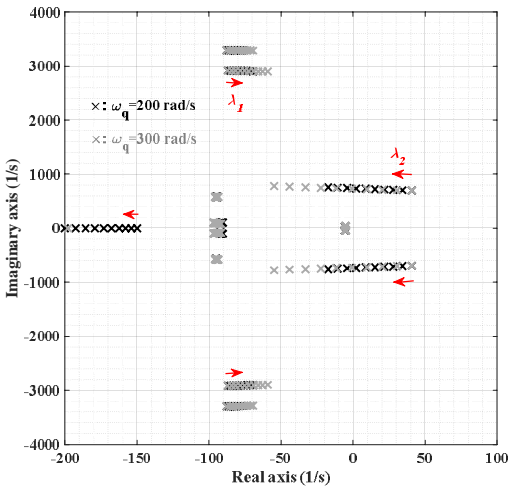


Fig. 8. The impact of  $y_{dd}^c(s)$  and  $y_{qq}^c(s)$  on the system dynamics.

Therefore, in weak grids where the DVI functionality makes the system unstable, the proposed compensators successfully stabilize the VSC controller.

## V. SIMULATION RESULTS

A time-domain simulation model is built for the grid-interactive VSC system of Fig. 1 in MATLAB to evaluate the preceding stability analyses and effectiveness of the proposed control technique. The detailed specifications of the model are presented in Appendix A. It is assumed that the maximum acceptable dc-link voltage deviation is 8%. Note that, the range of  $u_{dc}$  must be confined to  $[u_{dc}^{min}, u_{dc}^{max}]$  in which  $u_{dc}^{min}$  ensures the linear modulation operation of the converter and  $u_{dc}^{max}$  is determined by the voltage ratings of the converter switches [34]. The simulation type is discrete with a sampling time of 10  $\mu$ s.

### A. Uncompensated VSC Augmented with DVI Functionality

In this subsection, the VSC system responses without the proposed compensators are investigated. Fig. 9 illustrates the injected active and reactive power, and dc-link capacitor voltage when the active and reactive power references (i.e.  $P_{in}$  and  $i_q^*$ ) change by  $\pm 25\%$  and  $+100\%$ , respectively. This figure validates the proper operation of the grid-tied converter system under normal conditions of the power grid. As previously analyzed, however, the converter system augmented with the DVI functionality subjects to the instability when a frequency disturbance arises in weak grids. Note that, the DVI controller aims at primary frequency support by providing synthetic inertia. To depict the instability problem, a change (with the amplitude of -0.1 Hz) in the grid frequency is considered as a contingency and the results are presented in Fig. 10. It is clear that the active power, reactive power, and dc-link voltage attain their nominal values after a short time. However, the converter system becomes unstable when the frequency disturbance occurs at  $t=2$  s. Therefore, the supportive functionality introduced by the DVI concept makes the converter system unstable in weak grids, as indicated by the eigenvalue analyses of Section III.

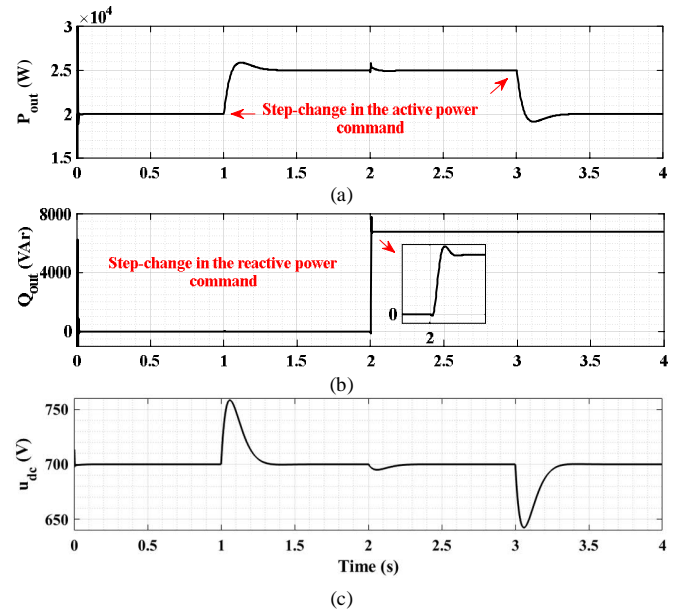


Fig. 9. (a) Active and (b) reactive power injection to the grid, (c) dc-link capacitor voltage, (notice the power grid is under normal operation).

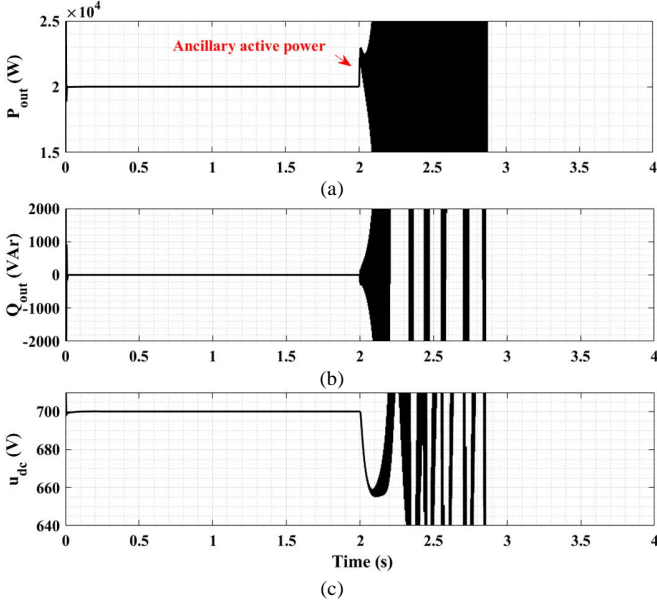


Fig. 10. (a) Injected active power, (b) reactive power, and (c) dc-link capacitor voltage when a grid frequency fluctuation occurs at  $t=2$  s.

### B. Compensated System

To overcome the instability problem arisen from the DVI technique in weak grids, the proposed compensator is implemented in the time-domain VSC model. Fig. 11 demonstrates the output active and reactive power of the VSC system considering a grid frequency disturbance ( $\Delta\omega = -2\pi \times 0.1$  Hz) at  $t=2$  s. As observed in Fig. 11(a), the injected active power to the grid rapidly increases from 20 kW to 22.8 kW when the perturbation occurs. This supplementary active power is equivalent to supplying virtual inertia to the power grid. Fig. 11(b) illustrates the reactive power exchange between the VSC system and the grid ( $Q_{out}$ ), where  $Q_{out}$  reaches approximately -700 VAr following the disturbance and then drops to zero at  $t=2.1$  s. The dc-link capacitor voltage is depicted in Fig. 11(c). As per this figure, the capacitor voltage drops to 650 V by the DVI controller (Fig. 4) and rebounds to the value of pre-perturbation when the grid frequency returns to 50 Hz. This means that the discharged energy by the dc-link capacitor supports the grid frequency, which is analogous to the released kinetic energy of real SGs. Moreover, the frequency oscillation measured by the PLL at the POI is presented in Fig. 12. This figure depicts that the VSC system augmented with the DVI function yields lower frequency nadir and the RoCoF level is improved by approximately 18% compared to the case in which the DVI loop is nullified. Hence, the frequency stability metrics (i.e. frequency nadir and RoCoF) are enhanced using the proposed approach. As previously stated, the compensation signals  $y_{dd}^c(s)$  and  $y_{qq}^c(s)$  are zero in the normal operation of the grid and do not change the accuracy of the controlled variables after disturbance.

Thus, compared to the uncompensated case (Fig. 10), the proposed compensation technique keeps the system completely stable in spite of providing ancillary active power for frequency support. It is worth mentioning that the supplementary active power provided by the DVI approach is 14% of the VSC power

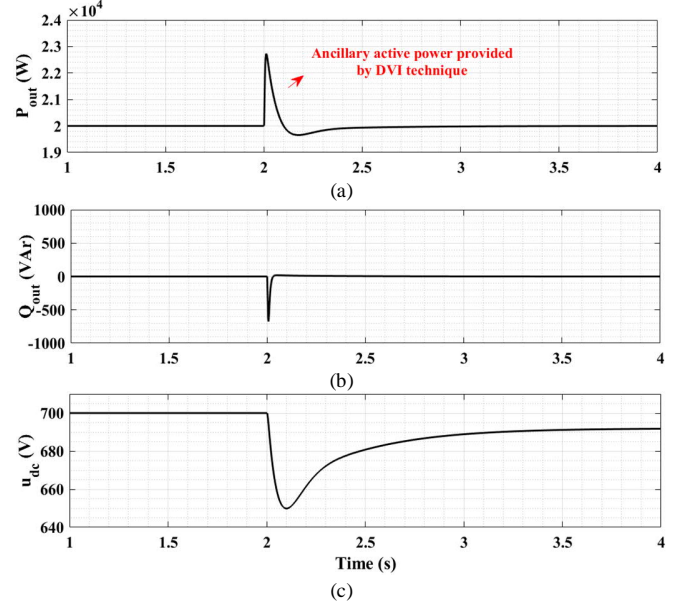


Fig. 11. (a) Active and (b) reactive power exchange with the power grid, (c) dc-link capacitor voltage (grid frequency disturbance occurs at  $t=2$  s).

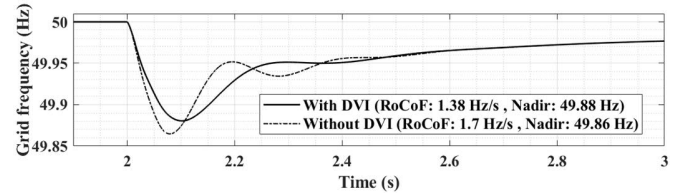


Fig. 12. Frequency oscillations measured by the PLL at the POI.

rating, which is a promising value for future power grids with significantly high levels of RESs penetration.

## VI. CONCLUSIONS

In this paper, a new control framework of grid-interactive VSC systems has been presented in detail. The VSC system under study is controlled in the current control mode, compositing of two conventional inner and outer control loops, the DVI controller and a novel compensator. The DVI technique can provide ancillary active power for the grid after frequency disturbances, which imposes a limit on the frequency fluctuations and slow down the grid frequency dynamic. It has been revealed that the coupling between  $d$ - and  $q$ - axis controllers defined by the DVI method gives rise to the system instability in weak grids. To overcome this instability problem and get the most benefit out of the acceptable dc-link capacitor voltage deviations, a novel compensation technique has been proposed and analyzed mathematically. The proposed compensator consists of two different signals, which are separately added to the  $d$ - and  $q$ - axis control loops. The auxiliary compensator signals are zero in steady state operation of the power grid. Hence, it does not alter the tracking of controlled variable commands. A time-domain simulation model of the system of interest has been built in MATLAB to confirm the analytical results and efficacy of the proposed compensation technique. The results have shown that the developed DVI approach can provide supplementary active power equal to 14% of the VSC power rating, which yields the

improvement of RoCoF following a grid frequency disturbance by approximately 18%. As a part of our future work, we apply the proposed control scheme to grid-interactive modular multilevel converters (MMCs) in power systems with high shares of RESs integrating through MMCs.

#### REFERENCES

- [1] J. Fang, H. Li, Y. Tang, and F. Blaabjerg, "On the Inertia of Future More-Electronics Power Systems," *IEEE Jour. Emerg. and Selec. Topics in Power Electron.*, vol. 7, no. 4, pp. 2130-2146, Oct. 2018.
- [2] J. Alipoor, Y. Miura, and T. Ise, "Power System Stabilization Using Virtual Synchronous Generator With Alternating Moment of Inertia," *IEEE Jour. Emerg. and Selec. Topics in Power Electron.*, vol. 3, no. 2, pp. 451-458, June 2015.
- [3] J. Fang, H. Li, Y. Tang, and F. Blaabjerg, "Distributed Power System Virtual Inertia Implemented by Grid-Connected Power Converters," *IEEE Trans. Power Electron.*, vol. 33, no. 10, pp. 8488-8499, Oct. 2018.
- [4] P. Energy, "Rate of Change of Frequency (ROCOF)-Review of TSO and Generator Submissions Final Report." *Commission for Energy Regulation (CER)*, May 2013.
- [5] D. Chowdhury, A. S. Md. Khalid Hasan, and M. Z. Rahman Khan, "Scalable DC Microgrid Architecture with Phase Shifted Full Bridge Converter Based Power Management Unit," *Int. Conf. Elec. and Comp. Engineering (ICECE)*, Bangladesh, pp. 22-25, 2018.
- [6] A. S. Md. Khalid Hasan, D. Chowdhury, and M. Z. Rahman Khan, "Scalable DC Microgrid Architecture with a One-Way Communication Based Control Interface," *Int. Conf. Elec. and Comp. Engineering (ICECE)*, Bangladesh, pp. 265-268, 2018.
- [7] A. S. M. K. Hasan, D. Chowdhury, and M. Z. R. Khan, "Performance Analysis of a Scalable DC Microgrid Offering Solar Power Based Energy Access and Efficient Control for Domestic Loads," *Int. Conf. Developments in Renewable Energy Technology (ICDRET)*, pp. 29-31, 2018.
- [8] D. Duckwitz, and B. Fischer, "Modeling and Design of  $df/dt$ -Based Inertia Control for Power Converters," *IEEE Jour. Emerg. and Selec. Topics in Power Electron.*, vol. 5, no. 4, pp. 1553-1564, Dec. 2017.
- [9] U. Bose, S. K. Chattopadhyay, C. Chakraborty, and B. Pal, "A Novel Method of Frequency Regulation in Microgrid," *IEEE Trans. Ind. Appl.*, vol. 55, no. 1, pp. 111-121, Jan.-Feb. 2019.
- [10] A. Sepehr, E. Pouresmaeil, M. Saedian, M. Routimo, and *et al.*, "Control of Grid-Tied Converters for Integration of Renewable Energy Sources into the Weak Grids," *International Conference on Smart Energy Systems and Technologies (SEST)*, Portugal, pp. 1-6, Sept. 2019.
- [11] H. Golpîra, A. R. Messina, and H. Bevrani, "Emulation of Virtual Inertia to Accommodate Higher Penetration Levels of Distributed Generation in Power Grids," *IEEE Trans. Power Systems*, vol. 34, no. 5, pp. 3384-3394, Sept. 2019.
- [12] S. Wang, and K. Tomsovic, "Fast Frequency Support From Wind Turbine Generators With Auxiliary Dynamic Demand Control," *IEEE Trans. Power Systems*, vol. 34, no. 5, pp. 3340-3348, Sept. 2019.
- [13] P. Vorobev, D. M. Greenwood, J. H. Bell, J. W. Bialek, and *et. al.*, "Deadbands, Droop, and Inertia Impact on Power System Frequency Distribution," *IEEE Trans. Power Systems*, vol. 34, no. 4, pp. 3098-3108, July 2019.
- [14] RoCoF Modification Proposal – TSOs' Recommendations, EirGrid/SONI, Ballsbridge, Ireland, 2012.
- [15] H. T. Nguyen, G. Yang, A. H. Nielsen, and P. H. Jensen, "Combination of Synchronous Condenser and Synthetic Inertia for Frequency Stability Enhancement in Low-Inertia Systems," *IEEE Trans. Sustainable Energy*, vol. 10, no. 3, pp. 997-1005, July 2019.
- [16] H. Beck, and R. Hesse, "Virtual Synchronous Machine," *9th International Conference on Electrical Power Quality and Utilization*, Barcelona, pp. 1-6, 2007.
- [17] Q. Zhong, and G. Weiss, "Synchronverters: Inverters That Mimic Synchronous Generators," *IEEE Trans. Ind. Electron.*, vol. 58, no. 4, pp. 1259-1267, Apr. 2011.
- [18] M. Ashabani, F. D. Freijedo, S. Golestan, and J. M. Guerrero, "Inducverters: PLL-Less Converters With Auto-Synchronization and Emulated Inertia Capability," *IEEE Trans. Smart Grid*, vol. 7, no. 3, pp. 1660-1674, May 2016.
- [19] N. Kakimoto, S. Takayama, H. Satoh, and K. Nakamura, "Power Modulation of Photovoltaic Generator for Frequency Control of Power System," *IEEE Trans. Energy Conversion*, vol. 24, no. 4, pp. 943-949, Dec. 2009.
- [20] J. Kim, V. Gevorgian, Y. Luo, M. Mohanpurkar, and *et al.*, "Supercapacitor to Provide Ancillary Services With Control Coordination," *IEEE Trans. Ind. Appl.*, vol. 55, no. 5, pp. 5119-5127, Sept. 2019.
- [21] E. Namor, F. Sossan, R. Cherkaoui, and M. Paolone, "Control of Battery Storage Systems for the Simultaneous Provision of Multiple Services," *IEEE Trans. Smart Grid*, vol. 10, no. 3, pp. 2799-2808, May 2019.
- [22] I. Serban, and C. Marinescu, "Control Strategy of Three-Phase Battery Energy Storage Systems for Frequency Support in Microgrids and with Uninterrupted Supply of Local Loads," *IEEE Trans. Power Electron.*, vol. 29, no. 9, pp. 5010-5020, Sept. 2014.
- [23] J. Fang, P. Lin, H. Li, Y. Yang, and *et al.*, "An Improved Virtual Inertia Control for Three-Phase Voltage Source Converters Connected to a Weak Grid," *IEEE Trans. Power Electron.*, vol. 34, no. 9, pp. 8660-8670, Sept. 2019.
- [24] E. Waffenschmidt, and R. S. Y. Hui, "Virtual Inertia with PV Inverters Using DC-link Capacitors," *18th European Conference on Power Electronics and Applications*, Germany, pp. 1-10, Sep. 2016.
- [25] B. K. Poolla, D. Groß, and F. Dörfler, "Placement and Implementation of Grid-Forming and Grid-Following Virtual Inertia and Fast Frequency Response," *IEEE Trans. Power Systems*, vol. 34, no. 4, pp. 3035-3046, July 2019.
- [26] B. K. Poolla, S. Bolognani and F. Dörfler, "Optimal Placement of Virtual Inertia in Power Grids," *IEEE Trans. Automatic Control*, vol. 62, no. 12, pp. 6209-6220, Dec. 2017.
- [27] Y. Huang, X. Yuan, J. Hu, and P. Zhou, "Modeling of VSC Connected to Weak Grid for Stability Analysis of DC-Link Voltage Control," *IEEE Jour. Emerg. and Selec. Topics in Power Electron.*, vol. 3, no. 4, pp. 1193-1204, Dec. 2015.
- [28] B. Wen, D. Boroyevich, R. Burgos, P. Mattavelli, and *et al.*, "Analysis of D-Q Small-Signal Impedance of Grid-Tied Inverters," *IEEE Trans. Power Electron.*, vol. 31, no. 1, pp. 675-687, Jan. 2016.
- [29] P. Kundur, "Power System Stability and Control," *McGraw-Hill Education*, 1<sup>st</sup> edition, 1994.
- [30] V. Kaura, and V. Blasko, "Operation of a Phase Locked Loop System under Distorted Utility Conditions," *IEEE Trans. Ind. Appl.*, vol. 33, no. 1, pp. 58-63, Jan. 1997.
- [31] W. Wu, Y. Chen, A. Luo, L. Zhou, and *et al.*, "A Virtual Inertia Control Strategy for DC Microgrids Analogized With Virtual Synchronous Machines," *IEEE Trans. Ind. Electron.*, vol. 64, no. 7, pp. 6005-6016, Jul. 2017.
- [32] M. Rasheduzzaman, J. A. Mueller, and J. W. Kimball, "An Accurate Small-Signal Model of Inverter-Dominated Islanded Microgrids Using  $dq$  Reference Frame," *IEEE Jour. Emerg. and Selec. Topics in Power Electron.*, vol. 2, no. 4, pp. 1070-1080, Dec. 2014.
- [33] F. D. Freijedo, E. Rodríguez-Díaz, M. S. Golsorkhi, J. C. Vasquez, and *et. al.*, "A Root-Locus Design Methodology Derived From the Impedance/Admittance Stability Formulation and Its Application for LCL Grid-Connected Converters in Wind Turbines," *IEEE Trans. Power Electron.*, vol. 32, no. 10, pp. 8218-8228, Oct. 2017.
- [34] D. G. Holmes, and T. A. Lipo, "Pulse Width Modulation for Power Converters: Principles and Practice," *John Wiley & Sons*, vol. 18, 2003.

#### APPENDIX A

The VSC system parameters are listed in the following table.

TABLE I. SYSTEM SPECIFICATIONS

Parameters	Values
$R_f, R_g$	0.056 $\Omega$ , 0.4 $\Omega$
$L_f, L_g$	1.35 mH, 2 mH
$C_f, C_{dc}$	50 $\mu$ F, 3 mF
$\omega_0$	$2\pi \times 50$ rad/s
$f_s$	10 kHz
$k, k_d$	30 V.s, 2.7 V.s
$k_q$	0.9 A/V
$\omega_{dr}, \omega_{dq}$	1500 rad/s, 300 rad/s
$k_{ppll}, k_{ppll}$	50, 3200
$k_{pdi}, k_{dii}$	0.2, 460
$k_{pui}, k_{dii}$	0.1, 50
$u_{dc}^*$	700 V
$P_m$	20 kW
$i_q^*$	0/11 A
$u_p (L-L)$	400 V

## APPENDIX B

The detailed small-signal representation of the uncompensated/compensated grid-tied VSC is provided in this appendix.

### A. Reference Frame Transformation

$$\begin{aligned}\begin{bmatrix} \Delta u_{pd}^c \\ \Delta u_{pq}^c \end{bmatrix} &= \begin{bmatrix} \Delta u_{pd} \\ \Delta u_{pq} \end{bmatrix} + \begin{bmatrix} U_{pq0} \\ -U_{pd0} \end{bmatrix} \Delta \delta \\ \begin{bmatrix} \Delta i_d^c \\ \Delta i_q^c \end{bmatrix} &= \begin{bmatrix} \Delta i_d \\ \Delta i_q \end{bmatrix} + \begin{bmatrix} I_{q0} \\ -I_{d0} \end{bmatrix} \Delta \delta \\ \begin{bmatrix} \Delta i_{wd}^c \\ \Delta i_{wq}^c \end{bmatrix} &= \begin{bmatrix} \Delta i_{wd} \\ \Delta i_{wq} \end{bmatrix} + \begin{bmatrix} I_{wq0} \\ -I_{wd0} \end{bmatrix} \Delta \delta \\ \begin{bmatrix} \Delta u_{td} \\ \Delta u_{tq} \end{bmatrix} &= \begin{bmatrix} \Delta u_{td}^c \\ \Delta u_{tq}^c \end{bmatrix} + \begin{bmatrix} -U_{tq0} \\ U_{td0} \end{bmatrix} \Delta \delta.\end{aligned}$$

### B. PLL

$$\begin{bmatrix} \Delta \dot{\delta} \\ \Delta \dot{\varphi}_\delta \end{bmatrix} = \begin{bmatrix} 0 & 1 \\ 0 & 0 \end{bmatrix} \begin{bmatrix} \Delta \delta \\ \Delta \varphi_\delta \end{bmatrix} + \begin{bmatrix} 0 & k_{ppll}/U_{pd0} \\ 0 & k_{ipll}/U_{pd0} \end{bmatrix} \begin{bmatrix} \Delta u_{pd}^c \\ \Delta u_{pq}^c \end{bmatrix}.$$

### C. DC-Bus

$$\Delta \dot{u}_{dc} = \frac{1}{C_{dc} u_{dc}^*} \left[ \Delta P_m - \frac{3}{2} (U_{pd0} \Delta i_d + I_{d0} \Delta u_{pd} + U_{pq0} \Delta i_q + I_{q0} \Delta u_{pq}) \right].$$

### D. LC Filter and Power Grid

$$\begin{aligned}\begin{bmatrix} \Delta i_{wd} \\ \Delta i_{wq} \end{bmatrix} &= \begin{bmatrix} 1/L_f & 0 \\ 0 & 1/L_f \end{bmatrix} \begin{bmatrix} \Delta u_{td} \\ \Delta u_{tq} \end{bmatrix} + \begin{bmatrix} -1/L_f & 0 \\ 0 & -1/L_f \end{bmatrix} \begin{bmatrix} \Delta u_{pd} \\ \Delta u_{pq} \end{bmatrix} \\ &+ \begin{bmatrix} -R_f/L_f & \omega_0 \\ -\omega_0 & -R_f/L_f \end{bmatrix} \begin{bmatrix} \Delta i_{wd} \\ \Delta i_{wq} \end{bmatrix} + \begin{bmatrix} I_{wq0} \left( \frac{k_{ppll}}{U_{pd0}} \Delta u_{pq}^c + \Delta \varphi_\delta \right) \\ -I_{wd0} \left( \frac{k_{ppll}}{U_{pd0}} \Delta u_{pd}^c + \Delta \varphi_\delta \right) \end{bmatrix} \\ \begin{bmatrix} \Delta \dot{u}_{pd} \\ \Delta \dot{u}_{pq} \end{bmatrix} &= \begin{bmatrix} 1/C_f & 0 \\ 0 & 1/C_f \end{bmatrix} \begin{bmatrix} \Delta i_{wd} \\ \Delta i_{wq} \end{bmatrix} + \begin{bmatrix} -1/C_f & 0 \\ 0 & -1/C_f \end{bmatrix} \begin{bmatrix} \Delta i_d \\ \Delta i_q \end{bmatrix} \\ &+ \begin{bmatrix} 0 & \omega_0 \\ -\omega_0 & 0 \end{bmatrix} \begin{bmatrix} \Delta u_{pd} \\ \Delta u_{pq} \end{bmatrix} + \begin{bmatrix} U_{pq0} \left( \frac{k_{ppll}}{U_{pd0}} \Delta u_{pq}^c + \Delta \varphi_\delta \right) \\ -U_{pd0} \left( \frac{k_{ppll}}{U_{pd0}} \Delta u_{pd}^c + \Delta \varphi_\delta \right) \end{bmatrix} \\ \begin{bmatrix} \Delta \dot{i}_d \\ \Delta \dot{i}_q \end{bmatrix} &= \begin{bmatrix} 1/L_g & 0 \\ 0 & 1/L_g \end{bmatrix} \begin{bmatrix} \Delta u_{td} \\ \Delta u_{tq} \end{bmatrix} + \begin{bmatrix} -R_g/L_g & \omega_0 \\ -\omega_0 & -R_g/L_g \end{bmatrix} \begin{bmatrix} \Delta i_d \\ \Delta i_q \end{bmatrix} \\ &+ \begin{bmatrix} I_{q0} \left( \frac{k_{ppll}}{U_{pd0}} \Delta u_{pq}^c + \Delta \varphi_\delta \right) \\ -I_{d0} \left( \frac{k_{ppll}}{U_{pd0}} \Delta u_{pd}^c + \Delta \varphi_\delta \right) \end{bmatrix}.\end{aligned}$$

### E. Inner-Loop Controller

$$\begin{bmatrix} \Delta u_{td}^c \\ \Delta u_{tq}^c \end{bmatrix} = \begin{bmatrix} \Delta u_{pd}^c - \omega_0 L_f \Delta i_{wq}^c + k_{pi} (\Delta i_d^* - \Delta i_d^c) \\ \Delta u_{pq}^c + \omega_0 L_f \Delta i_{wd}^c + k_{pi} (\Delta i_q^* - \Delta i_q^c) \\ \Delta u_{pq}^c + \omega_0 L_f \Delta i_{wd}^c + k_{pi} (\Delta i_q^* - \Delta i_q^c) \\ + \Delta \varphi_{id} - I_{wq0} L_f \left( \frac{k_{ppll}}{U_{pd0}} \Delta u_{pq}^c + \Delta \varphi_\delta \right) \\ + \Delta \varphi_{iq} + I_{wd0} L_f \left( \frac{k_{ppll}}{U_{pd0}} \Delta u_{pq}^c + \Delta \varphi_\delta \right) \end{bmatrix}$$

$$\begin{bmatrix} \Delta \dot{u}_{td}^{c*} \\ \Delta \dot{u}_{tq}^{c*} \end{bmatrix} = \begin{bmatrix} 2f_s (\Delta u_{td}^c - \Delta u_{td}^{c*})/3 \\ 2f_s (\Delta u_{tq}^c - \Delta u_{tq}^{c*})/3 \end{bmatrix}$$

$$\begin{bmatrix} \Delta \dot{\varphi}_{id} \\ \Delta \dot{\varphi}_{iq} \end{bmatrix} = \begin{bmatrix} k_{ii} (\Delta i_d^* - \Delta i_d^c) \\ k_{ii} (\Delta i_q^* - \Delta i_q^c) \end{bmatrix}.$$

### F. Outer-Loop Controller

$$\Delta i_d^* = k_{pu} \left[ \Delta u_{dc} - k \left( \frac{k_{ppll}}{U_{pd0}} \Delta u_{pq}^c + \Delta \varphi_\delta \right) \right] + \Delta \varphi_u$$

$$\Delta \dot{\varphi}_u = k_{iu} \left[ \Delta u_{dc} - k \left( \frac{k_{ppll}}{U_{pd0}} \Delta u_{pq}^c + \Delta \varphi_\delta \right) \right].$$

### G. The Proposed Compensator Model

$$\begin{aligned}A_{c4} &= \begin{bmatrix} -\omega_d & 0 \\ 0 & -\omega_q \end{bmatrix} \\ A_{c3} &= \begin{bmatrix} k_d \omega_d k_{ppll} & -k_q \omega_q \\ U_{pd0} & \end{bmatrix}^T \\ A_{c2} &= [k_d \omega_d \quad 0]^T \\ A_{c1} &= [-k_d \omega_d k_{ppll} \quad U_{pd0} k_q \omega_q]^T \\ C_c &= [1 \quad 1]^T.\end{aligned}$$

The final model of the uncompensated VSC system in state-space form is illustrated at the end of the next page, in which the elements  $a_{3,j}$  ( $j=1, 2, 8$ ),  $a_{4,j}$  ( $j=1, 8$ ),  $a_{6,8}$ ,  $a_{7,8}$ ,  $a_{10,8}$  and  $a_{13,1}$  in state matrix  $A_{uncomp}$  are equal to:

$$\begin{aligned}a_{3,1} &= 2f_s (U_{pq0} + \omega_0 I_{wd0} L_f + k k_{pu} k_{pi} k_{ppll} + I_{wq0} L_f k_{ppll} - I_{q0} k_{pi})/3 \\ a_{3,2} &= -2f_s (I_{wq0} L_f + k k_{pu} k_{pi})/3 \\ a_{3,8} &= -2f_s \left( \frac{k k_{pu} k_{pi} k_{ppll}}{U_{pd0}} + \frac{I_{wq0} L_f k_{ppll}}{U_{pd0}} \right)/3 \\ a_{4,1} &= 2f_s (\omega_0 I_{wq0} L_f + I_{d0} k_{pi} - I_{wd0} L_f k_{ppll} - U_{pd0})/3 \\ a_{4,8} &= 2f_s \left( 1 + \frac{I_{wd0} L_f k_{ppll}}{U_{pd0}} \right)/3 \\ a_{6,8} &= -\frac{1}{L_f} - \frac{I_{wd0} k_{ppll}}{U_{pd0}} \\ a_{7,8} &= \omega_0 + \frac{U_{pq0} k_{ppll}}{U_{pd0}}\end{aligned}$$

$$a_{10,8} = \frac{1}{L_g} - \frac{I_{d0}k_{ppll}}{U_{pd0}}$$

$$a_{13,1} = kk_{pu}k_{ii}k_{ppll} - I_{q0}k_{ii}.$$

$$[A_{m2}] = [0 \quad -k_{ii}].$$

$$B = \begin{bmatrix} 0_{2 \times 2} & \begin{bmatrix} \frac{4f_s k_{pi}}{9U_{pd0}} & 0 \\ 0 & \frac{2f_s k_{pi}}{3} \end{bmatrix} & 0_{2 \times 6} & \begin{bmatrix} \frac{1}{C_{dc}u_{dc}^*} & 0 \\ 0 & 0 \end{bmatrix} & \begin{bmatrix} \frac{2k_{ii}}{3U_{pd0}} & 0 \\ 0 & k_{ii} \end{bmatrix} \end{bmatrix}^T.$$

The state vector  $\Delta x_{comp}$  and state matrix  $A_{comp}$  correspond to the compensated VSC system are presented as follows, respectively:

$$[\Delta x_{comp}] = [\Delta x_{uncomp} \quad \Delta \gamma_{dd} \quad \Delta \gamma_{qq}]^T$$

$$A_{comp} = \begin{bmatrix} & & & & & 0_{4 \times 2} \\ & & & & & A_{m1} \\ & & & & & 0_{7 \times 2} \\ & & & & & A_{m2} \\ & & & & & \\ \hline A_{c1} & A_{c2} & 0_{2 \times 5} & A_{c3} & 0_{2 \times 6} & A_{c4} \end{bmatrix}_{16 \times 16}$$

where  $A_{mi}$  ( $i=1, 2$ ) are defined as:

$$[A_{m1}] = \begin{bmatrix} \frac{-1}{L_f} & 0 \\ 0 & \frac{-k_{pi}}{L_f} \end{bmatrix}$$

$$A_{uncomp} = \begin{bmatrix} -k_{ppll} & 1 & 0 & 0 & 0 & 0 & 0 & \frac{k_{ppll}}{U_{pd0}} & 0 & 0 & 0 & 0 & 0 & 0 \\ -k_{qpll} & 0 & 0 & 0 & 0 & 0 & 0 & \frac{k_{qpll}}{U_{pd0}} & 0 & 0 & 0 & 0 & 0 & 0 \\ a_{3,1} & a_{3,2} & -2f_s/3 & 0 & 0 & -2f_s\omega_0 L_f/3 & 2f_s/3 & a_{3,8} & -2f_s k_{pi}/3 & 0 & 2f_s k_{pu} k_{pi}/3 & 2f_s k_{pi}/3 & 2f_s/3 & 0 \\ a_{4,1} & 2f_s L_f I_{wd0}/3 & 0 & -2f_s/3 & 2f_s\omega_0 L_f/3 & 0 & 0 & a_{4,8} & 0 & -2f_s k_{pi}/3 & 0 & 0 & 0 & 2f_s/3 \\ -I_{wq0}k_{ppll} & I_{wq0} & \frac{1}{L_f} & 0 & -\frac{R_f}{L_f} & \omega_0 & -\frac{1}{L_f} & \frac{I_{wq0}k_{ppll}}{U_{pd0}} & 0 & 0 & 0 & 0 & 0 & 0 \\ I_{wd0}k_{ppll} & -I_{wd0} & 0 & \frac{1}{L_f} & -\omega_0 & -\frac{R_f}{L_f} & 0 & a_{6,8} & 0 & 0 & 0 & 0 & 0 & 0 \\ -U_{pq0}k_{ppll} & U_{pq0} & 0 & 0 & \frac{1}{C_f} & 0 & 0 & a_{7,8} & -\frac{1}{C_f} & 0 & 0 & 0 & 0 & 0 \\ U_{pd0}k_{ppll} & -U_{pd0} & 0 & 0 & 0 & \frac{1}{C_f} & -\omega_0 & -k_{ppll} & 0 & -\frac{1}{C_f} & 0 & 0 & 0 & 0 \\ -I_{q0}k_{ppll} & I_{q0} & 0 & 0 & 0 & 0 & \frac{1}{L_g} & \frac{I_{q0}k_{ppll}}{U_{pd0}} & -\frac{R_g}{L_g} & \omega_0 & 0 & 0 & 0 & 0 \\ I_{d0}k_{ppll} & -I_{d0} & 0 & 0 & 0 & 0 & 0 & a_{10,8} & -\omega_0 & -\frac{R_g}{L_g} & 0 & 0 & 0 & 0 \\ 0 & 0 & 0 & 0 & 0 & 0 & \frac{-3I_{d0}}{2C_{dc}u_{dc}^*} & \frac{-3I_{q0}}{2C_{dc}u_{dc}^*} & \frac{-3U_{pd0}}{2C_{dc}u_{dc}^*} & \frac{-3U_{pq0}}{2C_{dc}u_{dc}^*} & 0 & 0 & 0 & 0 \\ kk_{iu}k_{ppll} & -kk_{iu} & 0 & 0 & 0 & 0 & 0 & \frac{-kk_{iu}k_{ppll}}{U_{pd0}} & 0 & 0 & k_{iu} & 0 & 0 & 0 \\ a_{13,1} & -kk_{pu}k_{ii} & 0 & 0 & 0 & 0 & 0 & \frac{-kk_{pu}k_{ii}k_{ppll}}{U_{pd0}} & -k_{ii} & 0 & k_{ii}k_{pu} & k_{ii} & 0 & 0 \\ I_{d0}k_{ii} & 0 & 0 & 0 & 0 & 0 & 0 & 0 & 0 & -k_{ii} & 0 & 0 & 0 & 0 \end{bmatrix}_{14 \times 14}$$